



# Reactive fluid flow guided by grain-scale equilibrium reactions during eclogitization of dry crustal rocks

Sascha Zertani<sup>1,2</sup> · Timm John<sup>1</sup> · Caroline Brachmann<sup>1</sup> · Johannes C. Vrijmoed<sup>1</sup> · Oliver Plümper<sup>3</sup>

Received: 16 February 2022 / Accepted: 1 June 2022 / Published online: 15 June 2022  
© The Author(s) 2022

## Abstract

Fluid flow in crystalline rocks in the absence of fractures or ductile shear zones dominantly occurs by grain boundary diffusion, as it is faster than volume diffusion. It is, however, unclear how reactive fluid flow is guided through such pathways. We present a microstructural, mineral chemical, and thermodynamic analysis of a static fluid-driven reaction from dry granulite to ‘wet’ eclogite. Fluid infiltration resulted in re-equilibration at eclogite-facies conditions, indicating that the granulitic protolith was out of equilibrium, but unable to adjust to changing  $P$ – $T$  conditions. The transformation occurred in three steps: (1) initial hydration along plagioclase grain boundaries, (2) complete breakdown of plagioclase and hydration along phase boundaries between plagioclase and garnet/clinopyroxene, and (3) re-equilibration of the rock to an eclogite-facies mineral assemblage. Thermodynamic modelling of local compositions reveals that this reaction sequence is proportional to the local decrease of the Gibbs free energy calculated for ‘dry’ and ‘wet’ cases. These energy differences result in increased net reaction rates and the reactions that result in the largest decrease of the Gibbs free energy occur first. In addition, these reactions result in a local volume decrease leading to porosity formation; i.e., pathways for new fluid to enter the reaction site thus controlling net fluid flow. Element transport to and from the reaction sites only occurs if it is energetically beneficial, and enough transport agent is available. Reactive fluid flow during static re-equilibration of nominally impermeable rocks is thus guided by differences in the energy budget of the local equilibrium domains.

**Keywords** Reactive fluid flow · Lower continental crust · Dissolution–precipitation reactions · Local equilibrium · Eclogite

## Introduction

Metamorphism in orogenic roots or deeply subducting plates substantially impacts the geodynamic evolution of convergent plate boundaries because it results in considerable changes in the physical properties of the involved rocks (e.g., Austrheim 1991; Bedford et al. 2020; Dewey

et al. 1993; Hetényi et al. 2007; Klemd et al. 2011; Rondey et al. 2008; Zertani et al. 2022). These transformations reflect the changing  $P$ – $T$  conditions; however, many other factors play an essential role to facilitate and/or maintain metamorphic re-equilibration. Arguably, the most important factor is the availability of fluids during mineral reactions. Recently, for example, fluid-driven densification of the Philippine Sea slab has been invoked as a potential trigger for the swinging of the subducting plate preceding the magnitude 9.0 Tohoku-oki earthquake, illustrating the substantial impact that rapid fluid-mediated metamorphism may have on hazardous seismic events (Bedford et al. 2020). It has been demonstrated convincingly that these metamorphic reactions can be significantly overstepped in dry systems (e.g., Austrheim 1987; Jackson et al. 2004; Jamtveit et al. 2016; John and Schenk 2003; Wayte et al. 1989). However, when a fluid phase is introduced, reaction rates are accelerated, and mineral reactions occur to re-establish equilibrium between the rock composition, the fluid composition, and the prevailing  $P$ – $T$  conditions (Jamtveit et al. 2000; John and Schenk

---

Communicated by Othmar Müntener.

✉ Sascha Zertani  
sascha.zertani@mn.uio.no

✉ Timm John  
timm.john@fu-berlin.de

<sup>1</sup> Institute of Geological Sciences, Freie Universität Berlin, Berlin, Germany

<sup>2</sup> Njord Centre, Department of Geosciences, University of Oslo, Oslo, Norway

<sup>3</sup> Department of Earth Sciences, Utrecht University, Utrecht, the Netherlands

2003; Taetz et al. 2018). In this context, the efficiency of a fluid phase in driving metamorphic reactions forward is unequivocally linked with the generation of fluid pathways. However, most of the crustal rocks subjected to high-grade metamorphism consist of crystalline and nominally impermeable rocks (e.g., Manning and Ingebritsen 1999).

In this context, there is a consensus that brittle failure causes fluid pathways and that these often evolve into ductile shear zones that localize strain and channelize fluid flow (e.g., Austrheim 1987; Füsseis et al. 2009; Jamtveit et al. 2019; Mancktelow and Pennacchioni 2005; Menegon et al. 2017). Within these shear zones, fluid flow can be promoted by dynamically created permeability, where viscous grain-boundary sliding leads to the formation of porosity along grain boundaries (creep cavitation) thus providing a self-sustained mechanism for a granular fluid pump (Füsseis et al. 2009). Additionally, fluid flow in shear zones can be promoted by dissolution–precipitation creep (Wassmann and Stöckhert 2013), or possibly by fluid-pressure fluctuations (Kaatz et al. 2021).

However, fluid flow in those examples is intimately linked with ductile deformation. Nevertheless, it has been demonstrated that fluid migration through crustal rocks also occurs without associated deformation by viscous creep processes (e.g., Jamtveit et al. 2000; John and Schenk 2003; Mørk 1985; Plümper et al. 2017a; Putnis et al. 2021). In essentially impermeable rocks fluid flow is attributed to the generation of permeability by hydraulic or reaction-induced fracturing, densification reactions, diffusion along grain and phase boundaries, and interface-coupled dissolution and precipitation reactions (e.g., Ague and Axler 2016; Harlov et al. 2011; Hövelmann et al. 2010; Jamtveit et al. 2000; John and Schenk 2003; Oliver 1996; Plümper et al. 2012, 2017b; Putnis 2009; Putnis and Austrheim 2010; Putnis and John 2010). Recently, Wirth et al. (2021) detected partially open grain boundaries that can act as fluid conduits that were interpreted to result from an anisotropic thermoelastic response caused by the cooling of the rock. Similarly, fluid migration in feldspar has been linked with transient porosities that ensure that fluids are provided to the reaction front (Plümper et al. 2017a). Further, fluid migration into dry rocks was suggested to be driven by mineral reactions that cause disturbances in the local stress field leading to microfracturing (Jamtveit et al. 2000) or local pressure variations (Putnis et al. 2021).

It remains an important task to understand how fluid flow in such rocks is driven because it has been shown to affect large volumes of crustal rocks (e.g., John and Schenk 2003; Zertani et al. 2019), and occur on short timescales (Taetz et al. 2018; Beinlich et al. 2020), and thus has large-scale tectonic implications (Bedford et al. 2020). To tackle this issue, we present detailed microstructural investigations of an eclogitization front preserved within dry lower crustal

granulites from Holsnøy (Bergen Arcs, Western Norway). This sample was not affected by viscous deformation even during ongoing regional deformation, and the transformation is entirely static. We evaluate how the fluid-induced reaction front progressed into the dry granulite using mineral chemical data. Subsequently, we establish the succession in which the mineral reactions must have occurred, based on domains related to the availability of reactants at the grain and phase boundaries. These local compositions are then used to calculate the differences in Gibbs free energy between the dry and wet equilibrium assemblages for each characteristic reaction. We then compare the differences in Gibbs free energy to the sequence in which these reactions occur. In the context of reaction kinetics, these energies represent the reduction of the energy barrier. As a result, we demonstrate that the macroscopic fluid flow pattern in a static metamorphic setting is governed by the thermodynamics of local equilibria.

## Geological context

The exposures on the island of Holsnøy are part of the Lindås nappe, which belongs to the Bergen arc system (e.g., Austrheim 1987; Corfu et al. 2014). The island exposes pre-Caledonian granulite-facies basement rocks of the Baltica-affiliated Jotun microcontinent, which have been partially eclogitized during the Scandian phase of the Caledonian collision (e.g., Austrheim and Griffin 1985; Corfu et al. 2014; Jakob et al. 2019). Peak  $P$ – $T$ -conditions were reached at ~430 Ma (Glodny et al. 2008) and were determined to be 650–750 °C and 1.7–2.1 GPa (e.g., Bhowany et al. 2018; Jamtveit et al. 1990; Zhong et al. 2019).

Eclogitization was intimately linked with the availability of fluids and thus occurred locally, most prominently along shear zones (Austrheim 1987; Boundy et al. 1997; Raimbourg et al. 2005). The exposures feature shear zones on various scales ranging in width from a few centimeters to a few hundred meters, and the exposures can be regarded to represent a large-scale shear zone network established during high-pressure (HP) metamorphism in an orogenic root (Austrheim 1987, 1991; Jolivet et al. 2005; Zertani et al. 2019). Altogether, this shear zone network is a few kilometers wide and indicates overall top-E to top-NE kinematics (Raimbourg et al. 2005). The area between the shear zones preserves low-strain domains on variable scales, the largest of which is kilometer-sized (Zertani et al. 2019, Fig. 1).

The low-strain domains are composed either of preserved granulite or eclogite that has formed statically; however, in most cases, they feature a mixture of the two covering the entire spectrum from non-eclogitized to completely eclogitized. When eclogitization occurs statically (see Zertani et al. 2019 for details on static vs. dynamic eclogitization in Holsnøy) the reacted volume typically

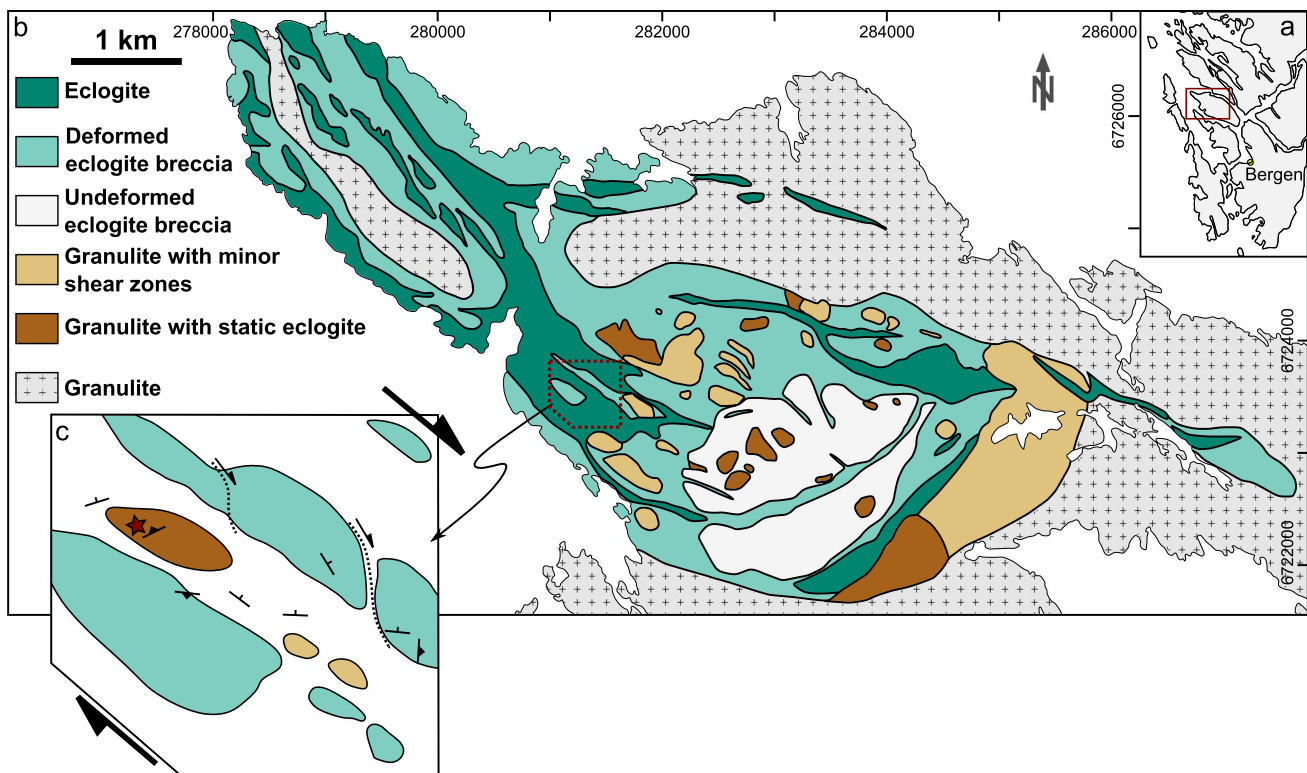


**Fig. 1** Geological map of northwestern Holsnøy. **a** The location of Holsnøy in western Norway. **b** The main structural and lithological associations that dominate the exposed shear zone network. **c** Magnification of the area where the sample was collected, providing folia-

tion measurements (from Zertani et al. 2019) and the sample location (red star). **a** and **b** are modified from (Zertani et al. 2020). The grid refers to UTM zone 32 N

forms finger-like domains, that are often parallel to the pre-existing granulite foliation (e.g., Jamtveit et al. 2000; Putnis et al. 2021; Zertani et al. 2019). Similar to the shear zones exposed in the same area the fluid is thought to initially enter the rock volume along fractures and be channelized along shear zones. However, when the eclogites are formed statically they display no signs of ductile deformation. With increasing size of these ‘eclogite fingers’, they interconnect and have nondescript and irregular shapes. However, it has been shown that the volume of statically formed eclogite on Holsnøy is substantial and thus an integral contribution to the overall volume of eclogitization (Zertani et al. 2019).

Although these exposures have been the target of a substantial number of studies, the source of the infiltrating fluids remains unclear. However, the dominant fluid must have been H<sub>2</sub>O-rich to produce the hydrous phases that are part of the eclogite-facies mineral assemblage (Jamtveit et al. 1990) and it has been suggested that they had a sedimentary source (Jamtveit et al. 2021; Matthey et al. 1994). In addition, it has also been demonstrated that the overall volume of infiltrating fluid must have been substantial (Kaatz et al. 2021).

## Methods

Our analyses were carried out on a sample approximately 30 × 10 × 8 cm in size composed of granulite, eclogite, and the transition between the two (Fig. 2). Six thin sections were prepared perpendicular to the reaction front covering the entire evolution from granulite to eclogite (Fig. 2).

Quantitative measurements of major element compositions of the rock-forming minerals were obtained using a JEOL JXA 8200 SuperProbe at Freie Universität Berlin, Germany. The beam was operated at an acceleration voltage of 15 kV, a beam current of 20 nA, and a beam diameter of 1 μm for garnet (Grt) and clinopyroxene (Cpx), 5 μm for zoisite (Zo)/clinozoisite (Czo), plagioclase (Pl), and amphibole (Amp) and 10 μm for phengite (Ph; mineral abbreviations throughout this study follow Whitney and Evans (2010) unless stated otherwise).

Each thin section (TS) was additionally mapped in the ZEISS automatic mineralogy lab at the Freie Universität Berlin using a ZEISS Gemini Sigma 300 Vp scanning electron microscope integrating two energy dispersive X-ray silicon drift detectors (Bruker Quantax XFlash

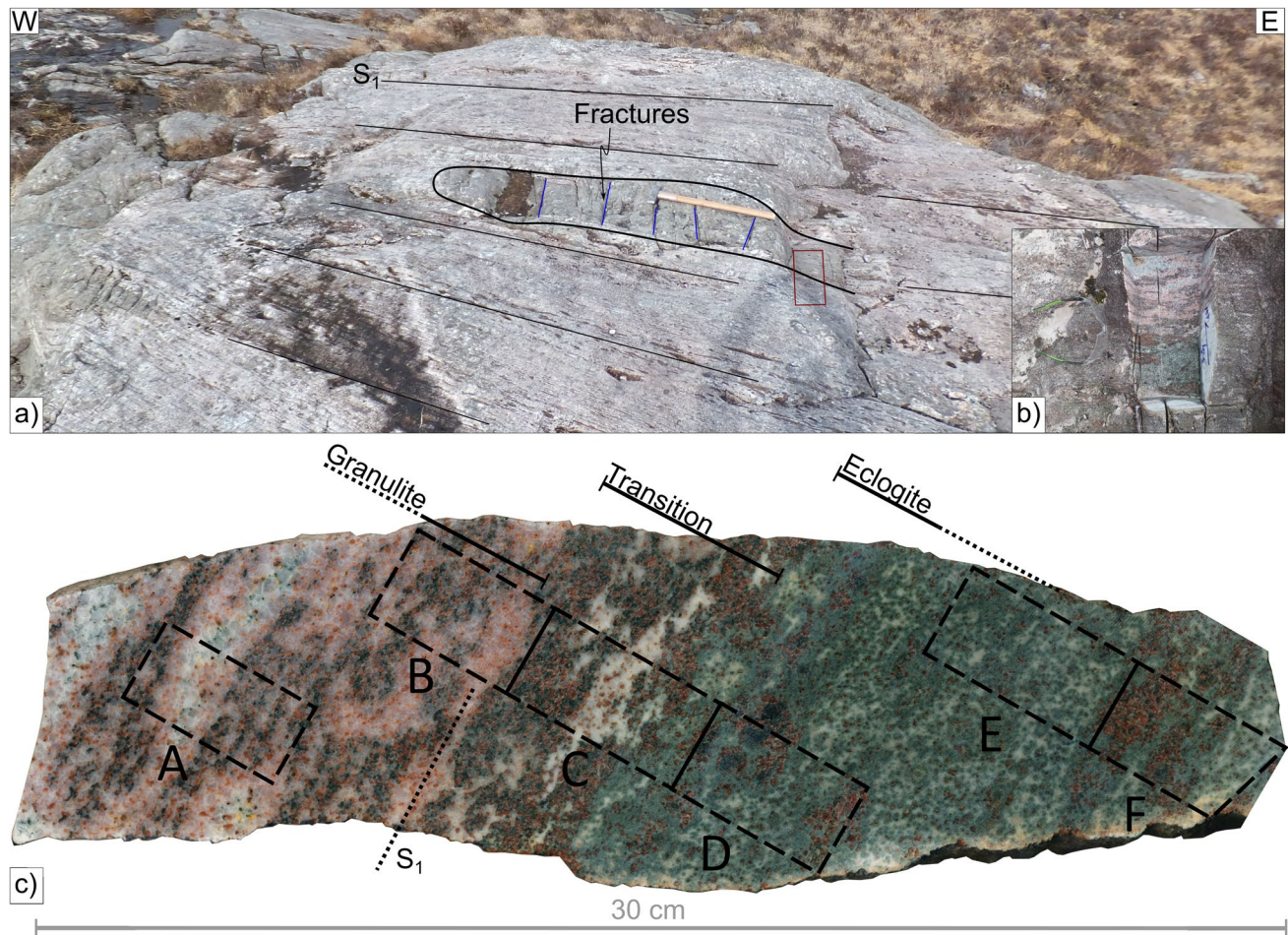


**Fig. 2** **a** Photograph of the sample location. The eclogite finger that was sampled is outlined with the black line and the granulite-facies foliation ( $S_1$ ) is traced by the thin black lines. Blue lines in the eclogite finger indicate extension fractures perpendicular to the long axis of the eclogite finger (see text for details). A hammer is in the center of the picture for scale. The red box shows the location of the extracted sample. **b** Sample location (red box in **a**) after sampling

showing the granulite (pink, bottom) and eclogite (green, top). Safety glasses are on the right side for scale. **c** Original slice of the sample used for analysis before thin section preparation. A–F indicates the thin sections that were prepared. The orientation of the granulite-facies foliation is indicated by  $S_1$ . The labels ‘Granulite’, ‘Transition’, and ‘Eclogite’ refer to the macroscopically visible rock features

6l60). The measurements were carried out with an acceleration voltage of 20 kV, an aperture size of 120  $\mu\text{m}$ , and a dwell time of 100 ms. A pixel size of 10  $\times$  10  $\mu\text{m}$  was used for thin sections B, C, D, and E; thin sections A and F were analyzed with a pixel size of 40  $\times$  40  $\mu\text{m}$  (Fig. 2).

Thermodynamic calculations were conducted using Thermolab (Vrijmoed and Podladchikov 2015, 2022) in the system. Compositions were input in mol considering the system Na–Ca–K–Fe–Mg–Al–Si–H–O. For the calculations, the following solution models were used: feldspar (Furman and Lindsley 1988), epidote, omphacite, garnet (Holland and Powell 1998), mica (Auzanneau et al. 2010; Coggon and Holland 2002), and amphibole (Dale et al. 2005).

## Sample description

### Outcrop description

The sample was collected from the Hundskjeftef area on northwestern Holsnøy (Fig. 1c; 32 N 281122 5723676). The main feature of the area is the Hundskjeftef shear zone network (e.g., Boundy et al. 1997; Raimbourg et al. 2005; Zertani et al. 2019), which preserves several low strain domains within. The sample was collected from one of these low strain domains (Fig. 2), characterized by a large (~250  $\times$  100 m in size) block of preserved granulite that exhibits only minor signs of eclogite-facies metamorphism

by a static overprint. We extracted the sample from one of the exposed ‘eclogite fingers’ (Fig. 2). This eclogitization feature extends parallel to the granulite-facies foliation and contains perpendicularly spaced extension fractures (Fig. 2). As these fractures are not associated with any mineral reactions and are only present within the eclogite, they are interpreted as late features unrelated to the eclogitization process itself, caused by mechanical differences between the eclogite and the granulite during decompression. The sample covers both the granulite and eclogite and preserves a macroscopically ~3 cm thick transition in between (Fig. 2b). On the outcrop scale, the main growth direction of this eclogitization feature is parallel to the pre-existing granulite foliation. A slice adjacent to the sample presented here was recently described in detail by Putnis et al. (2021), and our sample description thus focuses on those features relevant to our results.

### Granulite (thin sections A and B)

Thin sections A and B contain Pl (~60 vol%), Grt (~25 vol%), Cpx (~10 vol%), and minor spinel (Spl). They represent the unreacted (non-eclogitized) granulite, which is coarse-grained with grain sizes ranging from 0.5 to 2.0 mm. The granulite has a foliation formed by alternating, preferentially oriented aggregates of Grt and Cpx (Fig. 2). The thin sections also contain minor Zo/Czo, and kyanite (Ky; together ~5 vol%) that are the first products of the incipient eclogitization reaction.

Pl (~An<sub>42–45</sub>) is pinkish to white, and grain sizes range from 0.5 to 2.0 mm. Pl compositions are uniform throughout

both thin sections (Fig. 3). However, at the phase boundaries and along fractures the Pl is overgrown by symplectites of Zo/Czo needles (up to ~100 μm long) intergrown with K-feldspar (Kfs; Fig. 4a) while the adjacent Pl is more albitic (Fig. 3). The abundance of this overgrowth increases from thin section A to B.

Grt grains are typically isometric with grain sizes between 1.0 and 1.5 mm. The composition of the Grt in thin sections A and B is very homogeneous with Prp<sub>53–59</sub>Alm<sub>22–26</sub>Grs<sub>12–17</sub>Sp<sub>s0–1</sub> (Fig. 3) in the following Grt1. However, Grt boundaries are often frayed and surrounded by coronas of fine-grained (10–100 μm wide zones) omphacite (Omp) intergrown with Ky, Zo/Czo, and minor quartz (Qz) (Fig. 4a). Grt is zoned with thin Fe-rich rims around Grt1-type cores where these coronas occur. Grt boundaries are often straight at Fe-rich rims and sometimes feature 120° angles. These features are more commonly developed in Grt that shares phase boundaries with Pl rather than Cpx or other Grt.

Cpx occurs intergrown with Grt, forming coronas. Cpx grains are angular and euhedral to subhedral, ranging from 0.5 to 1.5 mm. Cpx has diopside (Di) to augite composition and is often fractured. Spl only occurs as a few single grains surrounded by corundum in thin section A, which are arranged along a ‘string’ parallel to the trend of the foliation.

### Transition zone (thin section C)

Thin section C covers the ~3 cm thick transition zone between the granulite and the eclogite (Fig. 5). Its dominant mineral assemblage is Grt (35 vol%) + Pl (25 vol%) + 2

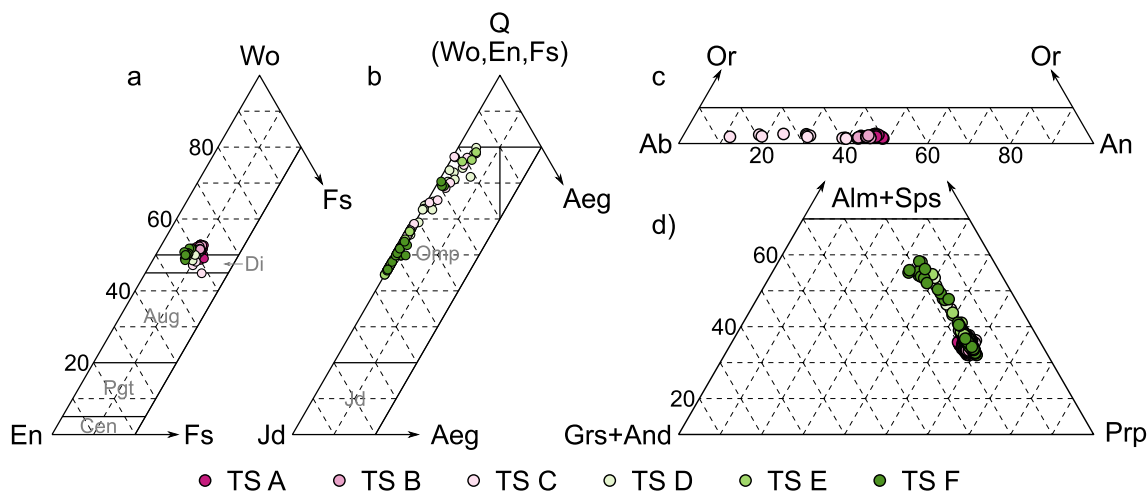


**Fig. 3** Results from electron microprobe analysis. **a** Triangular plot of Cpx1 measurements normalized to the end-members wollastonite (Wo), enstatite (En), and ferrosilite (Fs). **b** Triangle plot of Cpx2 measurements normalized to Q (Wo, En, Fs), jadeite (Jd), aegirine (Aeg) end-members. Classifications shown in **a** and **b** follow the rec-

ommendations of Morimoto (1988). **c** Triangle plot of Pl measurements. **d** Triangle plot of Grt measurements normalized to grossular + andradite (Grs + And), almandine + spessartine (Alm + Sps), and pyrope (Prp) components. Representative microprobe measurements are shown in Table 1. The color scheme from **a–d** is consistent

**Table 1** Representative electron microprobe analysis of Pl, Grt, and Cpx. Measurements are given in wt%, and mineral formulas were calculated based on 8 (Pl) and 12 (Grt) oxygens or 4 cations (Cpx)

Thin section	Pl		Grt1	Grt2	Cpx1	Cpx1/2	Cpx2
	A	C	A	F	B	C	F
Analyses	110	145	102	291	63	141	103
SiO <sub>2</sub>	56.46	63.36	41.27	39.52	48.45	53.10	55.32
Al <sub>2</sub> O <sub>3</sub>	27.45	23.36	22.16	20.96	10.87	8.60	13.18
Cr <sub>2</sub> O <sub>3</sub>	–	–	b.d.1	b.d.1	b.d.1	b.d.1	b.d.1
FeO	0.03	0.05	13.55	21.72	5.38	3.62	3.73
MnO	–	–	0.14	0.82	0.07	b.d.1	b.d.1
MgO	b.d.1	b.d.1	15.49	9.02	11.79	11.75	7.74
CaO	9.54	3.63	7.46	7.79	21.06	19.53	12.90
TiO <sub>2</sub>	b.d.1	b.d.1	0.08	b.d.1	0.54	0.33	0.16
Na <sub>2</sub> O	5.82	8.74	b.d.1	b.d.1	1.76	3.14	6.85
K <sub>2</sub> O	0.33	0.42	b.d.1	b.d.1	b.d.1	b.d.1	b.d.1
BaO	0.11	0.07	–	–	–	–	–
Total	99.74	99.62	100.15	99.83	99.90	100.08	99.86
	Normalized to 8 oxygens		Normalized to 12 oxygens		Normalized to 4 cations		
Si	2.54	2.81	3.00	3.01	1.77	1.91	1.96
Al	1.46	1.22	1.90	1.88	0.47	0.37	0.55
Cr	–	–	0.00	0.00	0.00	0.00	0.00
Fe <sup>2+</sup>	0.00	0.00	0.74	1.30	0.07	0.10	0.11
Fe <sup>3+</sup>	0.00	0.00	0.09	0.09	0.10	0.01	0.00
Mn	–	–	0.01	0.05	0.00	0.00	0.00
Mg	–	–	1.68	1.03	0.64	0.63	0.41
Ca	0.46	0.17	0.58	0.64	0.82	0.75	0.49
Ti	–	–	0.00	0.00	0.01	0.01	0.00
Na	0.51	0.75	0.00	0.00	0.12	0.22	0.47
K	0.02	0.02	0.00	0.00	0.00	0.00	0.00
Ba	0.00	0.00	–	–	–	–	–
Sum	4.99	4.97	8.00	8.00	4.00	4.00	4.00
Ab	51.47	79.34	55.70	32.28	10.2		
An	46.61	18.19	24.42	43.29	39.3		
Or	1.93	2.48	0.29	1.77	50.5		
			14.58	16.88		77.2	51.7
			4.34	4.35		22.2	48.3
			0.66	1.44		0.7	0.0

End-members were calculated using the procedure provided by Morimoto (1988) for pyroxene and Locock (2008) for Grt. End-members for feldspar were calculated by normalizing to total Na + K + Ca. Fe<sup>3+</sup> is calculated using the charge balance

Cpx (25 vol%) + Ph (5 vol.%) as well as Ky + Qz + Amp (all < 5 vol%) and Zo/Czo (< 1 vol%).

Macroscopically, it is mainly characterized by white Pl instead of the typical pinkish Pl of the granulite in thin sections A and B (Fig. 2). Microscopically, the abundance of tiny Zo/Czo and Ky needles with the addition of minor Qz grains associated with the Pl is significantly increased and not restricted to the grain boundaries but pervasively affects the Pl (Fig. 4b). Within the Pl grains, the symplectites composed of Zo/Czo needles intergrown

with Kfs ( $X_{Ep} = 0.02–0.10$ ) form a distinctive checkered pattern or occur as bundles associated with Ky needles; in rare cases tiny (< 2 μm) interstitial Qz is present. The reaction further causes the formation of more albitic Pl ( $X_{An} = 0.4–0.2$ ). The interior of Pl grains that are within or close to Grt–Cpx aggregates tend to be slightly less affected (Fig. 4b). These small mineral phases are heterogeneously distributed throughout the transition zone, and their abundance increases toward the eclogite. With this increase, the An-component of the Pl decreases down to An<sub>11</sub> (Fig. 3c).

Grt grains are associated with coronas of Omp, Ky, Zo/ Czo, and Ph, and thin Fe-rich rims, especially when the Grt is in contact with Pl, a feature that also increases toward the eclogite. In general, the Grt grain size decreases with increasing thickness of the surrounding corona. Grt compositions are, with the exclusion of the increasing thickness of Fe-rich rims, the same as in thin sections A and B (Fig. 3d).

Cpx has two distinct compositions: Di (Cpx1) and Omp (Cpx2). Cpx2 is significantly smaller than Cpx1, and Cpx1 dominantly occurs in aggregates with Grt, i.e., in the same microstructural position as in thin sections A and B, while Cpx2 occurs throughout the rock. However, Cpx2 preferentially also occurs associated with Grt as coronas around Grt grains (Fig. 3d). Additionally, Cpx1 is locally characterized by small (~10 µm) pores close to the boundary to newly formed Cpx2 (Fig. 4e). Thin rims of Amp (pargasite) are occasionally present where Cpx1 is in contact with Grt. Cpx2 compositions are variable but, a clear trend to higher Jd-contents is evident up to Jd<sub>53</sub> (Fig. 3b). Cpx–Pl phase boundaries are also lined by fine-grained Ph, Cpx2, and Czo with accessory rutile (Rt). All newly formed minerals have grain sizes < 100 µm. Ph occurs associated with Cpx2 around Grt or within the matrix associated with Czo and Ky and has low-celadonite contents of Si = 3.1–3.2 p.f.u.

### Eclogite (thin sections D, E, and F)

The dominant mineral assemblage of the eclogite is Grt (25 vol.%, Grt1 cores with Grt2 rims) + Omp (35 vol%, Cpx2) + Ky (10 vol.%) + Ph (10 vol%) + Qz (5 vol%) + Czo (< 5 vol%). Additionally, the thin sections contain ~15 vol% Cpx1. Accessory phases include Rt, pyrite, and apatite. The eclogite preserves traces of the granulite-facies foliation, defined by relicts of the Grt–Cpx aggregates, which are preserved but form no new foliation. Grain sizes are in the range of 10–200 µm, except for Grt and preserved Cpx1 grains, which are 0.3–1.2 mm in diameter.

Grt is zoned with the core composition resembling the composition of Grt1 (granulite facies) and the rims (40–80 µm thick) having higher Fe and lower Mg contents (Figs. 3d, 4). When in contact with Cpx2, Grt2 boundaries can be angular with ~120° angles.

Cpx2 is the most abundant mineral of the eclogite and occurs around remnants of large Cpx1 grains, coronas around Grt grains, and throughout the matrix. Cpx2 grain sizes range from 100 to 200 µm, and they can have small (< 3 µm) Rt inclusions. Their composition can reach values of up to ~Jd<sub>55</sub> (Fig. 3). Cpx1 is partly preserved in the eclogite as large grains associated with the Grt–Cpx aggregates. At their rims, however, the Jd-composition increases. Some Cpx1 grains also have fine amphibole lamellae that are too thin for precise microprobe measurements. The abundance of Cpx1 in sections D, E, and F seems to be unaffected by

the distance from the transition zone but is controlled by the abundance of Grt, i.e., where there is more Grt, more Cpx1 is preserved (Fig. 5). Symplectites of Pl and Amp commonly line the boundaries of Cpx2.

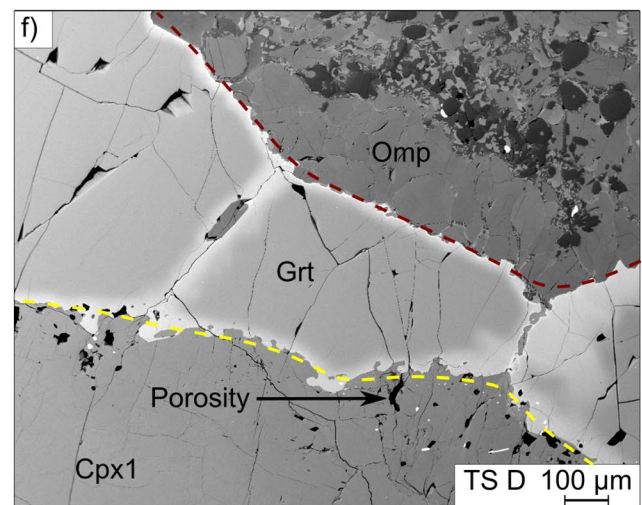
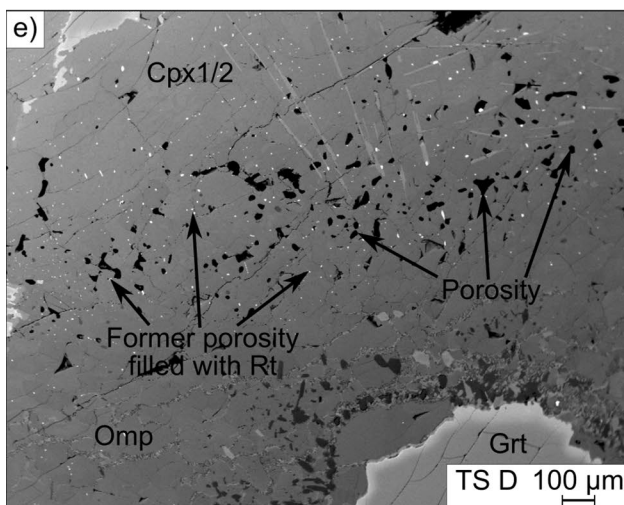
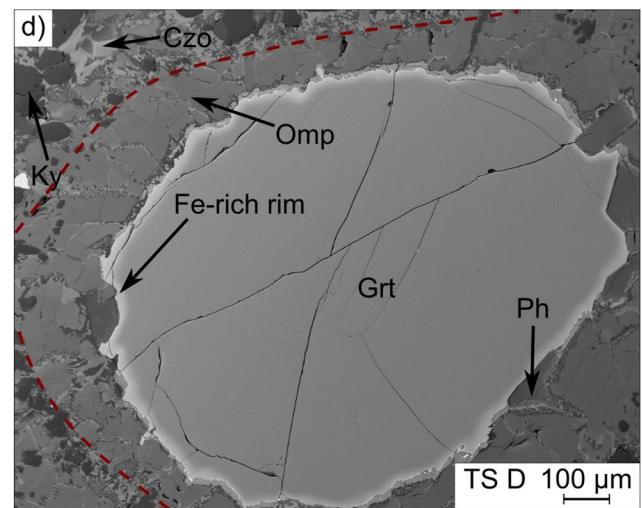
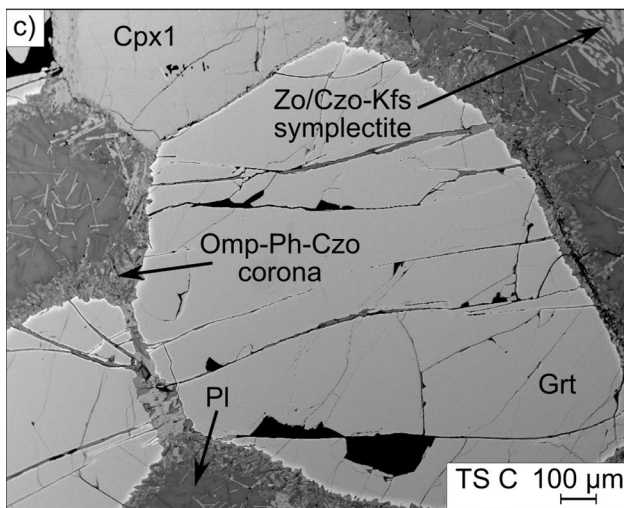
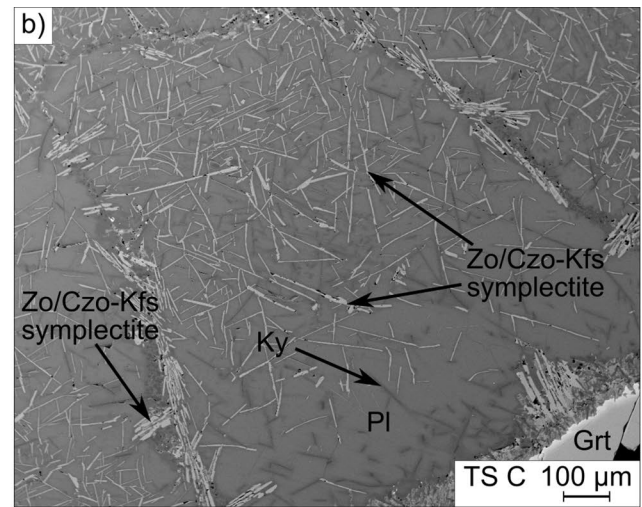
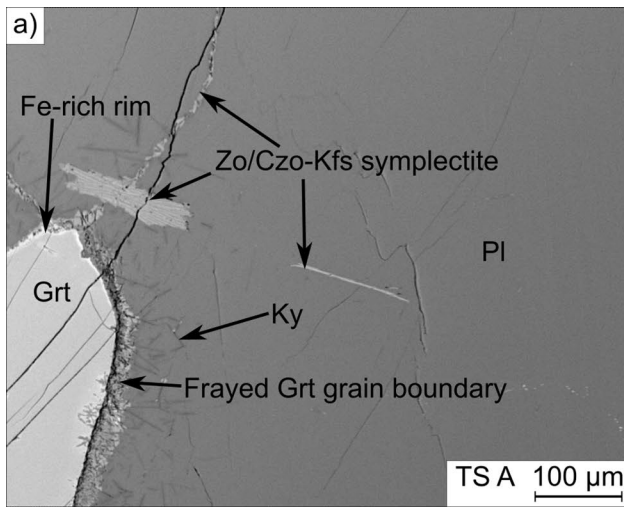
Czo occurs as elongate grains 100–500 µm long and ~50 µm wide. In the eclogite, Czo is zoned with increasing Fe and decreasing Ca contents outward. Their composition is in the range  $X_{Ep} = 0.01–0.14$ .

Low-celadonite Ph (Si = 3.1–3.2) occurs in the eclogite between Grt and Omp or as part of the eclogite matrix. Grain sizes are up to ~850 µm long and ~250 µm wide but are typically smaller when they occur within the matrix (grain size ~300 × 100 µm).

Ky occurs as round or elongated angular grains with a maximum long axis grain size of ~200 µm. Minor Qz occurs interstitially between all phases in the eclogite. Those parts of the fine-grained matrix closer to Grt are typically dominated by Cpx2, while Ph, Qz, and Czo occur as anastomosing aggregate trails in between.

### Thermodynamic modelling

The initially dry granulites of the lower crust are metastable at eclogite-facies conditions (e.g., Austrheim 1987; Jackson et al. 2004), and to overcome the energy barrier for re-equilibration to proceed requires sufficient time, additional energy such as heat, or an additional reactant that increases the rate at which the reactions occur, such as a fluid. To estimate the effect of the fluid on the local energy budget, we performed thermodynamic calculations using Thermolab (Vrijmoed and Podladchikov 2015, 2022). The stable mineral assemblage is calculated for each grain/phase boundary composition (two adjacent phases at each grain/phase boundary; Pl–Pl, Pl–Grt, Pl–Cpx, Grt–Grt, Grt–Cpx, and Cpx–Cpx) at 2 GPa and 700 °C (e.g., Bhowany et al. 2018) at dry (no H<sub>2</sub>O) and wet conditions (H<sub>2</sub>O in excess). For each calculation, the composition of the two adjacent grains/phases was considered as the bulk composition of the local system. One formula unit (e.g., 1 × Pl; K<sub>0.02</sub>Na<sub>0.52</sub>Ca<sub>0.46</sub>Si<sub>2.54</sub>Al<sub>1.46</sub>O<sub>8</sub>) per phase as normalized from the EMPA measurements was used as an input for the calculations (Fig. 6). As equilibrium thermodynamic calculations are size-independent, we can assume that considering local equilibrium at the grain/phase boundaries leads to a reasonable approximation above those scales where the surface energy of the crystal plays a significant role. For each calculated stable assemblage (dry and wet) and assuming a closed system, we calculate the Gibbs free energy (*G*). The difference between the two ( $\Delta G$ ) is considered as the energy benefit of the system for each specific reaction. The results reported in the following refer only to the energies and densities of the solids.



The calculated stable assemblages for each grain/phase boundary agree with those observed in the thin section (Table 2). The calculated change of  $G$  ( $\Delta G$ , solid) from the dry to the wet case at the specific grain/phase boundaries is

between zero, for grain/phase boundaries that do not include Pl and do not form hydrous phases, and  $-246.7 \text{ kJ} \times \text{mol}^{-1}$  for those that form hydrous phases. The absolute value of  $\Delta G$  is most significant for the Pl-Pl ( $-246.7 \text{ kJ} \times \text{mol}^{-1}$ )



**Fig. 4** Mircoprobe BSE images representative of the microstructures that characterize the fluid-driven transformation from granulite to eclogite. The thin section from which the images are derived is indicated in the lower right corner as ‘TS’. **a** Mostly unaffected granulite containing Pl and Grt. Pl is primarily unaffected except for Zo/Czo-Kfs-symplectites along grain boundaries. Grt features fine intergrowths at the contact to the Pl and a thin Fe-rich rim. **b** Pl close to the transition zone strongly perforated by Zo/Czo needles. Note the Zo/Czo has two preferential growth directions possibly mimicking the cleavage planes of the Pl. Zo/Czo-Kfs aggregates line Pl grain boundaries. **c** The width of the coronas surrounding Grt grains is increased (compared to a). Note that Cpx1-Pl and Grt-Pl phase boundaries are strongly affected by newly forming phases while the Cpx1-Grt phase boundary is not. **d** Omp corona around Grt (outlined by red dashed line) typical for the eclogite. The width of the Fe-rich rim of the Grt has increased slightly (compared to a and c). Grt has irregular boundaries, but locally they are straight (see right side). **e** Gradual transition from Cpx1 to Omp lined by holes (porosity). Bright spots are Rt grains that presumably filled the previously established porosity. **f** The upper right corner is completely converted to eclogite (above the dashed red line), while the lower-left corner preserves Cpx1 (below the yellow dashed line). Open pores line the contact between Cpx1 and Grt in the Cpx

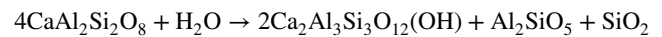
local compositions, followed by Pl–Cpx ( $-191.0 \text{ kJ} \times \text{mol}^{-1}$ ) and Pl–Grt ( $-4.5 \text{ kJ} \times \text{mol}^{-1}$ ) local compositions, proportional to the amount of hydrous phases being formed (Ep + Ph).

Similarly, the dry and wet cases result in different densities (only solid considered) of the stable mineral assemblage. This difference in density is most significant for the Pl-Pl local composition, with the density of the wet case being  $46 \text{ kg} \times \text{m}^{-3}$  lower than for the dry case. For the Pl–Cpx and Pl–Grt local compositions, this difference is minor with 1.8 and  $-1.1 \text{ kg} \times \text{m}^{-3}$ , respectively. Important is also the density change associated with the reaction itself (initial assemblage to stable assemblage). Considering the wet case only, the density of the Pl–Pl local composition increases most during the reactions ( $492.7 \text{ kg} \times \text{m}^{-3}$ ), followed by the Pl–Grt ( $303.4 \text{ kg} \times \text{m}^{-3}$ ), Pl–Cpx ( $255.5 \text{ kg} \times \text{m}^{-3}$ ), Grt–Cpx ( $73.1 \text{ kg} \times \text{m}^{-3}$ ), Cpx–Cpx ( $27.8 \text{ kg} \times \text{m}^{-3}$ ), and Grt–Grt ( $1.2 \text{ kg} \times \text{m}^{-3}$ ) local compositions. The results from the thermodynamic calculations are summarized in Table 2 and Fig. 6.

## Discussion

### Ahead of the main reaction front—initial stages of hydration

The first stage of hydration is characterized by the breakdown of Pl and the replacement by symplectites of Zo/Czo + Kfs along Pl grain boundaries, resulting in the formation of more albitic Pl (Figs. 4a, 5, 7). Here, Ca from Pl is released to form Zo/Czo by the reaction (Wayte et al. 1989):



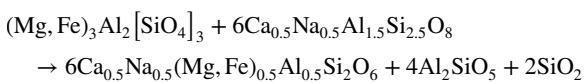
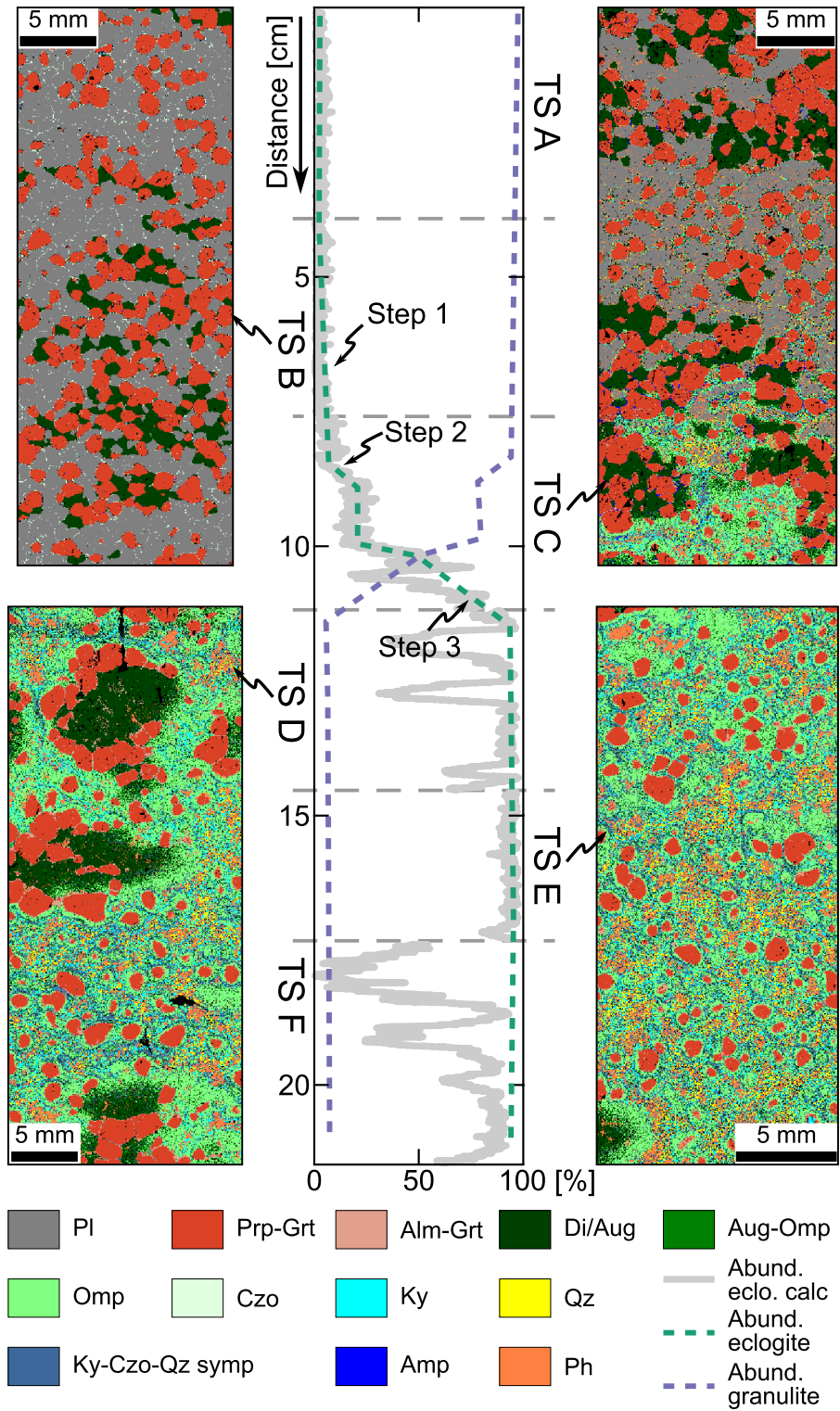
In our example, the minor K stored in the granulitic Pl is used to form Kfs, reducing the amount of Ky and Qz predicted by the reaction. Subsequently, the remaining Pl becomes progressively more albitic.

Such symplectites occur far ahead of the reaction front and are described in various studies on Holsnøy and elsewhere (e.g., Moore et al. 2019; Mørk 1985; Petley-Ragan et al. 2018; Putnis et al. 2021; Wayte et al. 1989), and have also been produced experimentally (Incel et al. 2019). Their abundance increases drastically with decreasing distance from the hydration front, and with increasing abundance, they also more frequently occupy the inner part of granulitic Pl grains forming a checkered pattern mimicking the Pl lattice structures (Fig. 4b). These observations agree with detailed studies of Pl breakdown in the presence of a fluid and the formation of Zo/Czo + albitic Pl from the Pl with < 10% of reaction progress (Wayte et al. 1989). The presence of these symplectites throughout most of the rock volume suggests that the entire rock was hydrated at least to some extent and subsequently that fluids were not restricted to those regions where eclogites have formed. However, the amount of fluid distributed throughout the rock volume must have been low compared to the fully eclogitized areas, resulting in only little reaction progress. This is supported by the observation that Kfs is present only in this part of our sample. Our models for the dry case that use Pl phase and grain boundaries all produce minor amounts of Kfs (Table 2), while all models for the wet case produce Ph. It follows, that the transient formation of Kfs indicates an initially limited availability of aqueous fluid. Additionally, we observe that the symplectites become more abundant and that they not only affect grain boundaries and fractures but also the interior of Pl grains closer to the eclogitization front. All of these symplectites are formed by dissolution–precipitation reactions between Pl and fluid. This indicates that the nearing eclogitization front progressively supplies more fluid that drives the reaction forward. The occurrence of the symplectites along grain boundaries suggest that the fluid preferentially infiltrates along there, while increasing abundance and the occurrence of the symplectites within Pl, closer to the reaction front suggests that the fluid content increases. The checkered pattern of symplectites inside the grains presumably mimics crystal planes of the Pl.

### At the reaction front—eclogitization

We define the beginning of the reaction front where the first Cpx2 grains occur along Pl grain boundaries. Cpx2 is most abundant at Pl–Grt phase boundaries forming from the Pl and the Mg and Fe-content of the Grt as illustrated in a simplified way by the reaction:

**Fig. 5** Evolution of the abundance of granulite and eclogite with respect to distance through the thin section series (center). Dashed horizontal lines show the transition between thin sections (TS A-F). For TS B-E, mineral distribution maps produced by SEM mapping are shown



Under the prevailing *P-T* conditions equilibration leads to more Fe-rich garnet compositions compared to the granulite-facies core, and the Cpx2 is thus more Mg-rich.

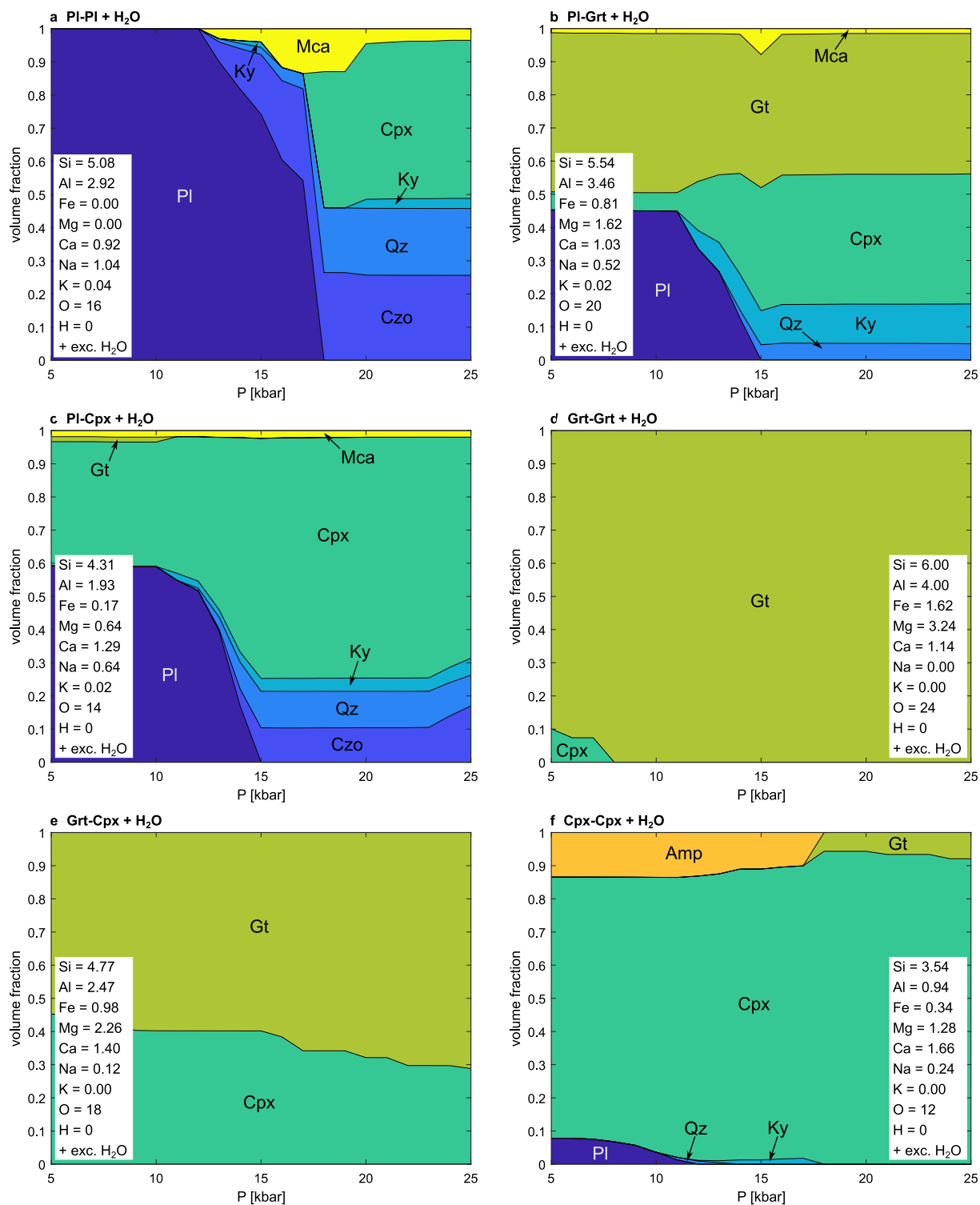


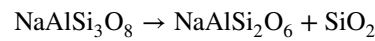
**Fig. 6** Calculated mineral assemblages for each grain boundary type at 700 °C as a function of pressure. The composition (in mol) used for each calculation is given in the white box in each diagram. Exc. – in excess. Mca – white mica

Cpx<sub>2</sub>, however, is also present along PI–PI and Cpx–PI grain and phase boundaries (Figs. 5, 7c). At PI–PI grain boundaries Cpx<sub>2</sub> is formed by the breakdown of the

remaining (now) albite-rich PI by a reaction such as (Wayte et al. 1989):

**Table 2** Results of thermodynamic calculations, including the initial assemblage and the calculated stable assemblages. Values for  $G$  are in  $\text{kJ} \times \text{mol}^{-1}$ . Stable assemblages,  $G$ , and  $\rho$  were calculated for 2 GPa and 700 °C (eclogite facies)

	Initial assemblage				Stable assemblage								$\rho$ [ $\text{kg}/\text{m}^3$ ]	$\Delta G$ [ $\text{kJ}/\text{mol}$ ]	$H$ [ $\text{kJ}/\text{mol}$ ]	$\Delta H$ [ $\text{kJ}/\text{mol}$ ]	$\rho$ [ $\text{kg}/\text{m}^3$ ]	$\Delta \rho_{(\text{stable-initial})}$ [ $\text{kg}/\text{m}^3$ ]
	Pl	Grt	Cpx	$\text{H}_2\text{O}$	Kfs	Ep	Qz	Ky	Amp	Grt	Ph	Cpx						
Pl-Pl	2				3	22	9			13		54	-2322.3	-2056.2	-216.6	3249.1	538.7	
Pl-Pl	2		in exc			26	20	3			5	47	-2569.0	-2272.8		3203.1	492.7	
Pl-Grt	1	1			1	5	12			43		39	-3551.6	-3125.0	-3.8	3538.2	304.5	
Pl-Grt	1	1	in exc			5	12			42	1	39	-3556.1	-3128.8		3537.1	303.4	
Pl-Cpx	1	1			2	13	4			2		80	-2583.5	-2275.2	-169.8	3279.4	253.7	
Pl-Cpx	1	1	in exc			10	11	4		68	2	73	-2774.5	-2445.0		3281.2	255.5	
Grt-Cpx		1								68		32	-4932.6	-4321.8	0.0	3622.2	73.1	
Grt-Cpx		1	in exc							68		32	-4932.6	-4321.8		3622.2	73.1	
Grt-Grt		2								100			-6333.4	-5546.2	0.0	3758.3	1.2	
Grt-Grt		2	in exc							100			-6333.4	-5546.2		3758.3	1.2	
Cpx-Cpx										6		94	-3359.1	-2946.1	0.0	3368.9	27.8	
Cpx-Cpx			in exc							6		94	-3359.1	-2946.1		3368.9	27.8	



However, this reaction would produce pure jadeite, which is not present in the sample, and thus transport of Fe and Mg to the reaction cite is required. This stepwise breakdown of Pl agrees with increasing reaction progress during eclogitization observed elsewhere (e.g., John and Schenk 2003; Mørk 1985; Wayte et al. 1989). Subsequently, the breakdown of Pl results in a sharp increase in reaction progress (Fig. 5). Local equilibrium calculations show that the reaction at Pl-Pl grain boundaries is associated with the highest absolute value of  $\Delta G$  from the dry to the wet case ( $-246.7 \text{ kJ} \times \text{mol}^{-1}$ ; i.e., the most significant energy gain) and that this is followed by Pl-Cpx and Pl-Grt phase boundaries ( $-191.0$  and  $-4.5 \text{ kJ} \times \text{mol}^{-1}$ ; Table 2). This reaction sequence agrees well with our microstructural observations that the Pl-Pl grain boundaries are the first to react to the availability of aqueous fluid (i.e., ahead of the main fluid front, Fig. 5), and after sufficient reaction progress, Cpx1 and Grt are increasingly incorporated into the eclogite equilibration.

At the Cpx-Pl phase boundaries, Cpx2 is produced by the dissolution of Cpx1 and precipitation of Cpx2. During this process, the Cpx2 is supplied with Na from the neighboring Pl (as well as some Al and Si), while Fe, Mg, and Ca are transported away from the reaction site (see also John and Schenk 2003).

The microstructural observations indicate that the grain/phase boundaries that do not feature Pl are involved in the reaction last, after which reaction progress rapidly reaches  $>90\%$  (Figs. 5, 7). These reactions are not associated with changes in  $G$  ( $\Delta G = 0 \text{ kJ} \times \text{mol}^{-1}$ ) because the stable assemblages calculated for the dry and wet case are identical. These reactions occur as the last step during eclogitization as they require the transport of Na to the reaction site to produce Cpx2, which leads to an energy benefit that makes these reactions favorable. It should be noted that the bulk reaction certainly results in minimized  $G$  compared to the metastable granulite assemblage. Similarly, the calculations of Grt-Grt local compositions indicate that Grt is the most stable phase at that particular local composition, and no reaction would occur. Especially, because the eclogite-facies Grt (higher Fe) can only form if a reaction partner allows Mg exchange such as Cpx2. As also the grain size of the re-equilibrating Grt decreases it follows that these grain boundaries have a low tendency to react if they are not supplied by Na to form Cpx2.

$\Delta G$  varies significantly depending on the local compositions, resulting in a stepwise reaction guided by the energy benefit provided by specific local reactions. Subsequently, the eclogite has a strongly inhomogeneous distribution of the newly formed phases that generally agrees with the local assemblages expected from thermodynamic calculations

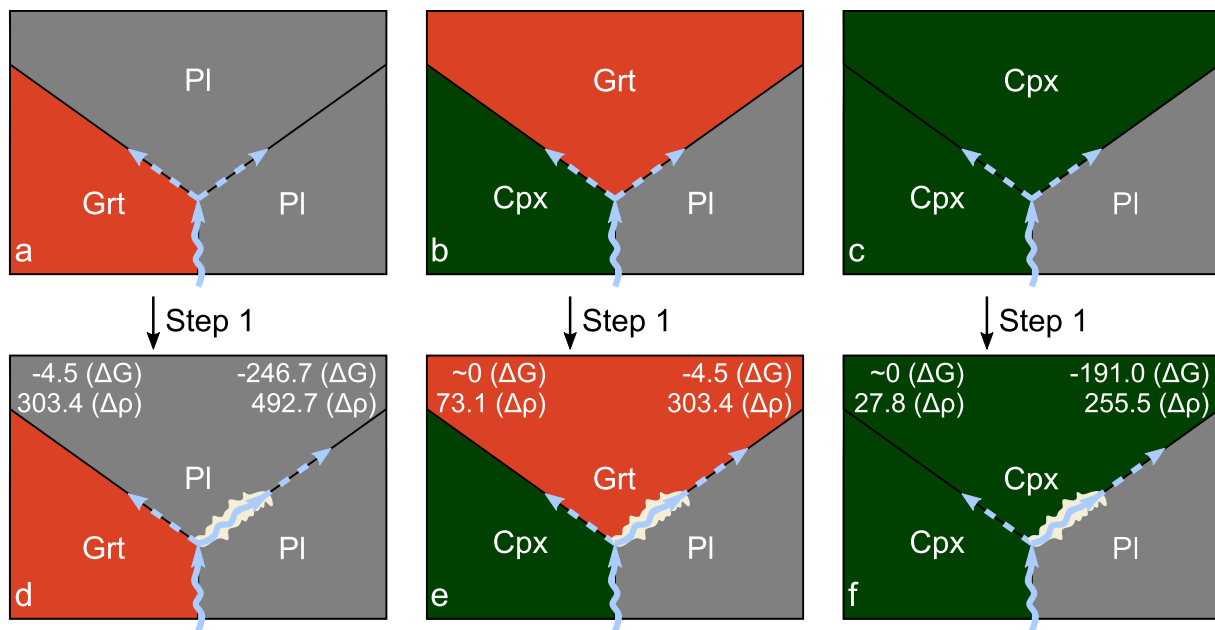


**Fig. 7** Sketch showing the initial grain/phase boundaries (a–c) and the resulting reaction progress of step 1 of the reaction sequence (d–f) described in the text.  $\Delta G$  (in  $\text{kJ} \times \text{mol}^{-1}$ ) and  $\Delta \rho$  (in  $\text{kg} \times \text{m}^{-3}$ ) for each grain/phase boundary assemblage are provided in panels d–f.

(Figs. 5, 6), indicating that element transport was limited to those instances (discussed above) where it was energetically beneficial for the product assemblages.

### In the wake of the reaction front

Some remnants of the granulite protolith are still preserved after the main reaction front has passed. This observation mainly concerns large grains of Cpx1. Similarly, John and Schenk (2003) reported that the last remnants of gabbros in the Zambezi Belt (Zambia) are Cpx, indicating the general validity of this reaction sequence. However, lamellae of amphibole (see Putnis et al. (2021) for detailed description) and remnants of porosity (Fig. 4) found in the remaining Cpx1 indicate that Cpx1 is not at bulk equilibrium conditions. Such grains are preserved in association with abundant Grt, which acts as a barrier against the advancing fluid front due to their low reactivity. Preserved Cpx within Grt-coronas with open pores has recently also been described from the eclogite type locality at Hohl (Eastern Alps, Austria; Rogowitz and Huet 2021). The Grt rim is partially dissolved and enriched in Fe, and this new Grt composition establishes local equilibrium conditions with the adjacent minerals, evidenced by straight boundaries at 120° angles (Fig. 4d). Afterwards, the compositional change within the Grt grains is likely dominated by volume diffusion, which was too slow to affect the Grt cores (Pollok et al. 2008; Raimbourg et al. 2007). Using diffusion modeling of Grt

Blue dashed arrows symbolize grain boundary diffusion of the infiltrating fluid, the yellow area represents a reaction halo along the preferred reaction pathway, and the solid blue arrow symbolized further fluid flow enabled by reaction-induced porosity

profiles Raimbourg et al. (2007) estimated the timescales of eclogite re-equilibration on Holsnøy to be on the order of hundreds to thousands of years.

Furthermore, the propagation of finger-like structures (Fig. 2) has been described to occur dominantly parallel to the granulite-facies foliation (Jamtveit et al. 2000; Putnis et al. 2021; Zertani et al. 2019). Our results show that this is caused by the Grt–Cpx aggregates that form the foliation. Essentially, the reaction front propagation is slowed down by Grt forming barriers with low reactivity for the given P, T, X conditions. Consequently, the reactivity of the phases present along grain and phase boundaries guides the fluid/reaction progress toward the energetically most beneficial direction, and the local energy budget is thus crucial in determining its path.

### Control on reaction progress

Our results suggest that the eclogitization reaction takes place in three steps (Fig. 8): (1) The entire rock volume is at least partially hydrated, as is evidenced by the widespread occurrence of Zo/Czo–Kfs symplectites along PI grain boundaries and within the interior of granulitic PI closer to the main reaction front, and the concurrent increase in albite content of PI. (2) The complete breakdown of PI, which results in the growth of Cpx2 (Omp) along grain boundaries. (3) The remaining reactions to complete the conversion into an eclogite. While step 1 occurs without any element

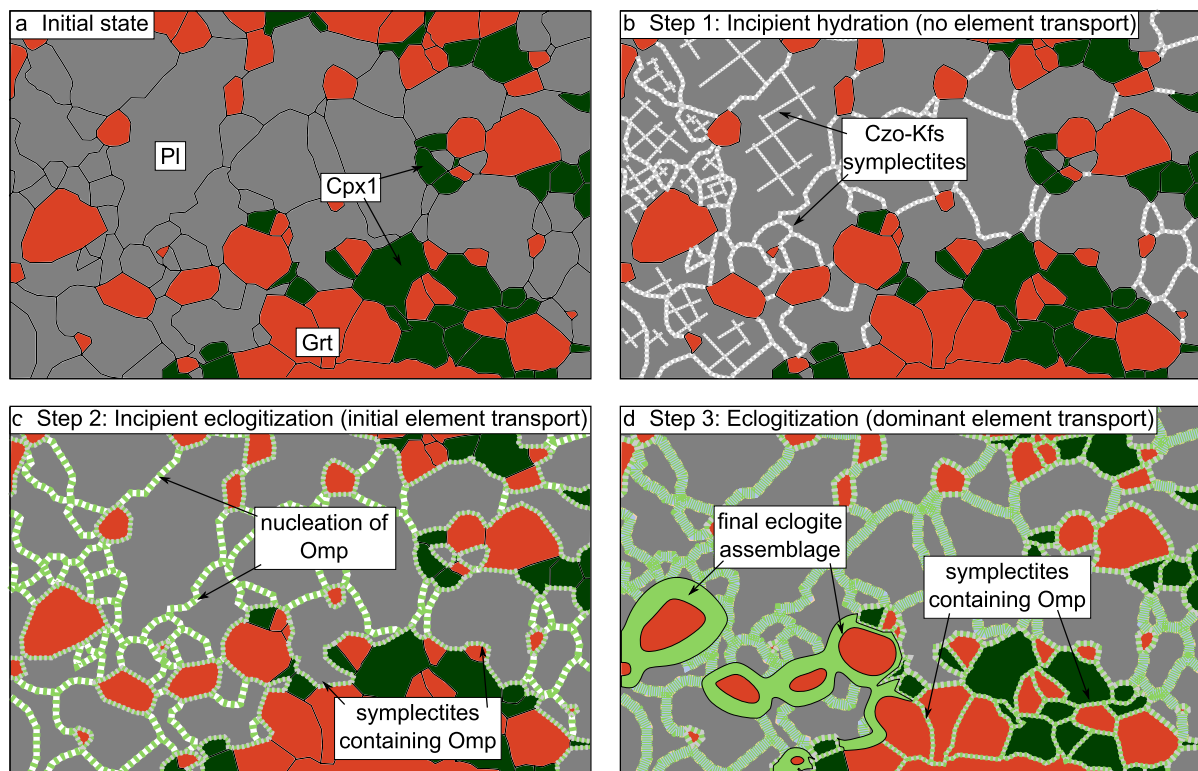


**Fig. 8** Sketch of the initial granulite and the changes associated with each step of the reaction. **a** Initial granulite microstructure. **b** Incipient hydration with symplectites of Zo/Czo-Kfs + albitic Pl along Pl-Pl grain boundaries and later throughout the Pl grains. For simplicity, the Zo/Czo-Kfs symplectites within the grains are only shown in **b**, where they form and are omitted in the following images. **c** Incipi-

ent eclogitization indicated by the nucleation of Omp along all grain/phase boundaries adjacent to Pl. **d** Eclogitization by the formation of symplectites containing Cpx2 (Omp) along the remaining grain/phase boundaries and Cpx2 coronas around Grt. For the final microstructure of the eclogite the reader is referred to Fig. 5

redistribution, transport of mainly Na, Mg, and Fe becomes increasingly important in steps 2 and 3.

The growth of metamorphic minerals depends on the changes in the free energy of the reaction ( $\Delta G_r$ ), the interfacial energies ( $\Delta G_{inf}$ ), and the strain energy ( $\Delta G_{strain}$ ; Philpotts and Ague 2022). As the transformation described here is static  $\Delta G_{strain}$  is negligible. Furthermore, Gaidies and George (2021) quantified  $\Delta G_{inf}$  for garnet nucleation. They conclude that  $\Delta G_{inf}$  can play a significant role in that reaction rates are higher at smaller grain sizes. However, they also conclude that  $\Delta G_{inf}$  becomes a controlling factor if the driving force for nucleation is small, and the system is close to equilibrium. Additionally,  $\Delta G_{inf}$  is typically on the order of  $J \times mol^{-1}$ , while the  $\Delta G$  calculated here is on the orders of  $kJ \times mol^{-1}$  (Gaidies et al. 2011; Gaidies and George 2021). It follows that interfacial energies will not play a significant role in our step 1 and step 2, as the reactions are highly overstepped. It is likely that this influence increases in step 3, which is supported by the observation that the last remnants that survive are generally large Cpx1

grains. Consequently,  $\Delta G_{inf}$  seems to only have a significant effect after the reaction pattern in our example has already been established.

The infiltration of the fluid causes  $\Delta G_r$  to become more negative (increase in magnitude) by the  $\Delta G$  calculated in the present study. These calculations indicate that the reaction sequence is controlled by the energy benefit associated with the individual reactions leading to eclogitization and the required element transport. In general, we estimate the local decrease in G to be  $\sim 250 kJ \times mol^{-1}$  for step 1,  $\sim 5\text{--}200 kJ \times mol^{-1}$  for step 2, and  $> 0 kJ \times mol^{-1}$  for step 3. Before the reactions occur, the granulite is metastable, and reactions are highly overstepped. The observation that the reactions occur only after fluid infiltration indicates that the fluid reduces the energetical barrier to overcome, i.e., the activation energy. We consider an Arrhenius-type relationship (Philpotts and Ague 2022):

$$\text{Reaction rate} \propto \exp\left(\frac{-\Delta G_a}{RT}\right), \quad (1)$$

where  $\Delta G_a$  is the Gibbs free energy of activation,  $R$  is the gas constant, and  $T$  is the temperature.

Additionally, in the framework of the growth of metamorphic minerals, i.e., metamorphic reactions,  $\Delta G_a$  is proportional to the ratio of  $\Delta G_{\text{inf}}^3/\Delta G^2$  (e.g., Philpotts and Ague 2022; Gaidies et al. 2011). That means for the given case where  $\Delta G_{\text{inf}}$  is negligible and  $\Delta G$  is highly negative,  $\Delta G_a$  becomes smaller and the reaction rate thus increases. Furthermore, the Gibbs energy in the final stage of the wet case is lower than in the dry case. With reference to the same initial stage, i.e., the metastable dry granulite, it follows that more energy is released during the reaction, by an amount proportional to  $\Delta G$  (see  $\Delta H$  in Table 2). Note that the  $\Delta H$  given in Table 2 refers to the enthalpy difference between the dry and the wet case, but not to the change from initial to product assemblage. This later latent heat release has been estimated for the reaction with the largest  $\Delta G$  (Pl–Pl) to be  $\sim 10\text{--}13 \text{ kJ} \times \text{mol}^{-1}$  (Incel et al. 2019; Holland 1980). Assuming a heat capacity for Pl at 700 °C of  $\sim 250 \text{ J} \times \text{mol}^{-1}$  (Berman and Brown 1985) this results in a local temperature increase of  $\sim 40\text{--}50 \text{ °C}$  at the site where the symplectites form. In the Arrhenius-type equation (Eq. 1) both the increase in temperature and the reduction of the activation energy will lead to higher reaction rates. Clearly, the energy budget will be modified by element transport (e.g., Na, Mg, Fe). However, our microstructural and mineral chemical observations suggest that element transport, apart from the aqueous fluid, was limited to the extent necessary to provide the most effective energy gain and the calculated values can thus be considered as minimum estimates. Additionally, previous studies indicate that the overall transformation to eclogite on Holsnøy occurs without significant change in the bulk chemical composition (Centrella 2019), and the necessary elements must, therefore, be derived locally.

With the local energy budget at the grain and phase boundaries as a guide for fluid flow in the deep crust it remains to answer what drives the fluid forward. Assuming a system like the one described here an aqueous fluid along, for example, a Pl–Pl grain boundary and a Cpx–Cpx grain boundary will most likely facilitate reactions at both sites. However, because the reaction at the Pl–Pl grain boundary is more beneficial it occurs more rapidly while leading to a density increase (i.e. porosity formation) leaving room for new fluid to enter the site driving the reaction forward by continuously providing an interface between fluid and unreacted material. Over time this leads to significantly more reaction progress than at other sites, as observed here (Fig. 5). Additionally, the increase in density associated with the Pl–Pl grain boundary is significantly larger than for the others. The density increase at the different grain/phase boundaries also follows a similar trend as it does for  $\Delta G$  (Table 2). This local density increase results in reaction-induced porosity formation along grain/phase boundaries

within the dissolving Pl (Plümper et al. 2017a; Hövelmann et al. 2010).

These results provide a model for how fluid flow is guided through the rock volume. In itself, this model is dependent on the availability of a fluid. The exact fluid source on Holsnøy is still a matter of debate but fluid inclusion evidence indicates a sedimentary source (Mattey et al. 1994). The fluids have infiltrated along (seismic) fractures and caused re-equilibration of the rock along shear zones (Austrheim 1987). Oliver (1996) suggested that if deformation terminates abruptly this can lead to pervasive fluid flow away from the shear zones. Similarly, considering that the ductile shear zones are weak zones an established pressure gradient (Mancktelow 2002) would cause fluids to be expelled from the shear zones, and could explain the formation of eclogite fingers (Jamtveit et al. 2000). Further, Putnis et al. (2021), recently suggested that the local pressure in the eclogite finger itself could be higher than in the surrounding. All of these possibilities are compatible with the model we present here.

The presented model further opens potential implications for other hydration scenarios. Serpentinization reactions for example have also been described to occur in distinct sequences (e.g., Schwarzenbach et al. 2016). Similarly, minor hydration of seismic faults in ophiolitic peridotite and gabbro show that hydration occurs along fractures in the Pl, while Cpx has escaped re-equilibration (Pennacchioni et al. 2020). These are only two examples that highlight that our model can potentially be applied to other settings.

In summary, the energy budget of the individual mineral reactions along grain/phase boundaries has a strong influence on the reaction progress. Accordingly, the local reactions that are energetically most beneficial occur first. Subsequent reactions are then regulated by the energy budget in conjunction with the availability of the necessary elements to reach the most stable local mineral assemblage. This suggests that reactive fluid flow may be guided by differences in the energy balance between local compositions.

## Conclusions

This study presents a detailed microstructural analysis of a preserved reaction front. From these results the following conclusions are drawn:

1. The transformation from granulite to eclogite studied here is entirely static and does not involve any deformation. The eclogitization reaction takes place in three steps: (i) Initial hydration along Pl grain boundaries by the formation of Zo/Czo-Kfs symplectites and increasing albite-content in Pl. (ii) Complete breakdown of Pl and growth of symplectites containing Omp (Cpx<sub>2</sub>), first along Pl phase and grain boundaries and then

increasingly also affecting the interior of Pl. (iii) The complete transformation to the eclogite mineral assemblage. These steps are controlled by the local energy gain associated with the reaction between the infiltrating fluid and the local mineral assemblages directly adjacent to the grain and phase boundaries; i.e., reactions that are energetically more favorable occur first.

2. Element transport is limited to those sites where it results in an energy benefit during the reaction and becomes increasingly important in steps 2 and 3. At the same time, the release of elements (Na, Mg, Fe) necessary for these reactions is controlled by the energy benefit of the releasing reaction.
3. The density increase associated with the reactions supports the established reaction sequence by the formation of transient porosity. An interface between fluid and unreacted material is thus continuously provided driving the reaction forward.
4. As the energetically more beneficial reactions occur first and the same reactions are associated with the largest formation of porosity they further provide new sites for the fluid to facilitate reactions. The net fluid flux is thus guided by the sequence of reactions. As a result, small differences in the energy balance within a rock can act as a guiding mechanism for reactive fluid flow.

**Acknowledgements** We thank Andrew Smye and one anonymous reviewer as well as the handling editor Othmar Müntener for their thorough comments that significantly improved the quality of this contribution. For loan of the rock saw during fieldwork, we thank Alexander Prent and Kamini Bhowany. This research was supported by the Deutsche Forschungsgemeinschaft (DFG) through grant CRC 1114 “Scaling Cascades in complex Systems”, Project Number 235221301, Project (C09) – “Dynamics of rock dehydration on multiple scales”. Oliver Plümper is supported by an ERC Starting Grant (nanoEARTH, 852069).

**Funding** Open Access funding enabled and organized by Projekt DEAL. This research was supported by the Deutsche Forschungsgemeinschaft (DFG) through grant CRC 1114 “Scaling Cascades in complex Systems”, Project Number 235221301, Project (C09) – “Dynamics of rock dehydration on multiple scales”. O. Plümper was supported by an ERC starting Grant (“nanoEARTH”; 852069).

**Availability of data and material** All data that was used in this study is provided in the manuscript.

**Code availability** Not applicable.

## Declarations

**Conflict of interest** No conflicts of interest.

**Studies involving humans and/or animals** Not applicable.

**Ethics approval** not applicable.

**Consent to participate/publication** All listed authors consent to the publication of this article.

**Open Access** This article is licensed under a Creative Commons Attribution 4.0 International License, which permits use, sharing, adaptation, distribution and reproduction in any medium or format, as long as you give appropriate credit to the original author(s) and the source, provide a link to the Creative Commons licence, and indicate if changes were made. The images or other third party material in this article are included in the article's Creative Commons licence, unless indicated otherwise in a credit line to the material. If material is not included in the article's Creative Commons licence and your intended use is not permitted by statutory regulation or exceeds the permitted use, you will need to obtain permission directly from the copyright holder. To view a copy of this licence, visit <http://creativecommons.org/licenses/by/4.0/>.

## References

- Ague JJ, Axler JA (2016) Interface coupled dissolution-precipitation in garnet from subducted granulites and ultrahigh-pressure rocks revealed by phosphorous, sodium, and titanium zonation. *Am Miner* 101(7):1696–1699. <https://doi.org/10.2138/am-2016-5707>
- Austrheim H (1987) Eclogitization of lower crustal granulites by fluid migration through shear zones. *Earth Planet Sci Lett* 81(2):221–232. [https://doi.org/10.1016/0012-821X\(87\)90158-0](https://doi.org/10.1016/0012-821X(87)90158-0)
- Austrheim H (1991) Eclogite formation and dynamics of crustal roots under continental collision zones. *Terra Nova* 3(5):492–499. <https://doi.org/10.1111/j.1365-3121.1991.tb00184.x>
- Austrheim H, Griffin WL (1985) Shear deformation and eclogite formation within granulite-facies anorthosites of the Bergen Arcs, western Norway. *Chem Geol* 50(1–3):267–281. [https://doi.org/10.1016/0009-2541\(85\)90124-X](https://doi.org/10.1016/0009-2541(85)90124-X)
- Auzanneau E, Schmidt M, Vielzeuf D, Connolly JD (2010) Titanium in phengite: a geobarometer for high temperature eclogites. *Contrib Miner Petrol* 159:1. <https://doi.org/10.1007/s00410-009-0412-7>
- Bedford JR, Moreno M, Deng Z, Oncken O, Schurr B, John T, Báez JC, Bevis M (2020) Months-long thousand-kilometre-scale wobbling before great subduction earthquakes. *Nature* 580(7805):628–635. <https://doi.org/10.1038/s41586-020-2212-1>
- Beinlich A, John T, Vrijmoed JC, Tominaga M, Magna T, Podladchikov YY (2020) Instantaneous rock transformations in the deep crust driven by reactive fluid flow. *Nat Geosci* 13(4):307–311. <https://doi.org/10.1038/s41561-020-0554-9>
- Berman RG, Brown TH (1985) Heat capacity of minerals in the system Na<sub>2</sub>O–K<sub>2</sub>O–CaO–MgO–FeO–Fe<sub>2</sub>O<sub>3</sub>–Al<sub>2</sub>O<sub>3</sub>–SiO<sub>2</sub>–TiO<sub>2</sub>–H<sub>2</sub>O–CO<sub>2</sub>: representation, estimation, and high temperature extrapolation. *Contrib Miner Petrol* 89:168–183. <https://doi.org/10.1007/BF00379451>
- Bhowany K, Hand M, Clark C, Kelsey DE, Reddy SM, Pearce MA, Tucker NM, Morrissey LJ (2018) Phase equilibria modelling constraints on *P–T* conditions during fluid catalysed conversion of granulite to eclogite in the Bergen Arcs, Norway. *J Metamorph Geol* 36(3):315–342. <https://doi.org/10.1111/jmg.12294>
- Boundy TM, Mezger K, Essene EJ (1997) Temporal and tectonic evolution of the granulite-eclogite association from the Bergen Arcs, western Norway. *Lithos* 39(3):159–178. [https://doi.org/10.1016/S0024-4937\(96\)00026-6](https://doi.org/10.1016/S0024-4937(96)00026-6)
- Centrella S (2019) The granulite- to eclogite- and amphibolite-facies transition: a volume and mass transfer study in the Lindås Nappe, Bergen Arcs, west Norway. *Geol Soc Lond Spec Publ* 478:241–264. <https://doi.org/10.1144/SP478.9>



- Coggon R, Holland TJB (2002) Mixing properties of phengitic micas and revised garnet-phengite thermobarometers. *J Metamorph Geol* 20(7):683–696. <https://doi.org/10.1046/j.1525-1314.2002.00395.x>
- Corfu F, Andersen TB, Gasser D (2014) The Scandinavian Caledonides: main features, conceptual advances and critical questions. *Geol Soc Lond Spec Pub* 390:9–43. <https://doi.org/10.1144/sp390.25>
- Dale J, Powell R, White RW, Elmer FL, Holland TJB (2005) A thermodynamic model for Ca–Na clin amphiboles in Na<sub>2</sub>O–CaO–FeO–MgO–Al<sub>2</sub>O<sub>3</sub>–SiO<sub>2</sub>–H<sub>2</sub>O–O for petrological calculations. *J Metamorph Geol* 23(8):771–791. <https://doi.org/10.1111/j.1525-1314.2005.00609.x>
- Dewey JF, Ryan PD, Andersen TB (1993) Orogenic uplift and collapse, crustal thickness, fabrics and metamorphic phase changes: the role of eclogites. *Geol Soc Lond Spec Pub* 76:325–343. <https://doi.org/10.1144/GSL.SP.1993.076.01.16>
- Furman ML, Lindsley DH (1988) Ternary-feldspar modeling and thermometry. *Am Mineral* 73(3–4):201–215
- Fusseis F, Regenauer-Lieb K, Liu J, Hough RM, De Carlo F (2009) Creep cavitation can establish a dynamic granular fluid pump in ductile shear zones. *Nature* 459:974–977. <https://doi.org/10.1038/nature08051>
- Gaidies F, George FR (2021) The interfacial energy penalty to crystal growth close to equilibrium. *Geology* 49(8):988–992. <https://doi.org/10.1130/G48715.1>
- Gaidies F, Pattison DRM, de Capitani C (2011) Toward a quantitative model of metamorphic nucleation and growth. *Contrib Miner Petrol* 162:975–993. <https://doi.org/10.1007/s00410-011-0635-2>
- Glodny J, Kühn A, Austrheim H (2008) Geochronology of fluid-induced eclogite and amphibolite facies metamorphic reactions in a subduction–collision system, Bergen Arcs, Norway. *Contrib Miner Petrol* 156:27–48. <https://doi.org/10.1007/s00410-007-0272-y>
- Harlov DE, Wirth R, Hetherington CJ (2011) Fluid-mediated partial alteration in monazite: the role of coupled dissolution–reprecipitation in element redistribution and mass transfer. *Contrib Miner Petrol* 162(2):329–348. <https://doi.org/10.1007/s00410-010-0599-7>
- Hetényi G, Cattin R, Brunet F, Bollinger L, Vergne J, Nábělek JL, Diamant M (2007) Density distribution of the India plate beneath the Tibetan plateau: geophysical and petrological constraints on the kinetics of lower-crustal eclogitization. *Earth Planet Sci Lett* 264(1–2):226–244. <https://doi.org/10.1016/j.epsl.2007.09.036>
- Holland TJB (1980) The reaction albite = jadeite+quartz determined experimentally in the range 600–1200 °C. *Am Miner* 65(1–2):129–134
- Holland TJB, Powell R (1998) An internally consistent thermodynamic data set for phases of petrological interest. *J Metamorph Geol* 16(3):309–343. <https://doi.org/10.1111/j.1525-1314.1998.00140.x>
- Hövelmann J, Putnis A, Geisler T, Schmidt BC, Golla-Schindler U (2010) The replacement of plagioclase feldspars by albite: observations from hydrothermal experiments. *Contrib Miner Petrol* 159:43–59. <https://doi.org/10.1007/s00410-009-0415-4>
- Incel S, Labrousse L, Hilalret N, John T, Gasc J, Shi F, Wang Y, Andersen TB, Renard F, Jamtveit B, Schubnel A (2019) Reaction-induced embrittlement of the lower continental crust. *Geology* 47(3):235–238. <https://doi.org/10.1130/G45527.1>
- Jackson JA, Austrheim H, McKenzie D, Priestley K (2004) Metastability, mechanical strength, and the support of mountain belts. *Geology* 32(7):625–628. <https://doi.org/10.1130/g20397.1>
- Jakob J, Andersen TB, Kjöll HJ (2019) A review and reinterpretation of the architecture of the South and South-Central Scandinavian Caledonides—a magma-poor to magma-rich transition and the significance of the reactivation of rift inherited structures. *Earth Sci Rev* 192:513–528. <https://doi.org/10.1016/j.earscirev.2019.01.004>
- Jamtveit B, Bucher-Nurminen K, Austrheim H (1990) Fluid controlled eclogitization of granulites in deep crustal shear zones, Bergen arcs, Western Norway. *Contrib Miner Petrol* 104(2):184–193. <https://doi.org/10.1007/bf00306442>
- Jamtveit B, Austrheim H, Malthe-Sorensen A (2000) Accelerated hydration of the Earth's deep crust induced by stress perturbations. *Nature* 408(6808):75–78. <https://doi.org/10.1038/35040537>
- Jamtveit B, Austrheim H, Putnis A (2016) Disequilibrium metamorphism of stressed lithosphere. *Earth Sci Rev* 154:1–13. <https://doi.org/10.1016/j.earscirev.2015.12.002>
- Jamtveit B, Petley-Ragan A, Incel S, Dunkel KG, Aupart C, Austrheim H, Corfu F, Menegon L, Renard F (2019) The effects of earthquakes and fluids on the metamorphism of the lower continental crust. *J Geophys Res Solid Earth* 124:7725–7755. <https://doi.org/10.1029/2018jb016461>
- Jamtveit B, Dunkel KG, Petley-Ragan A, Austrheim H, Corfu F, Schmid DW (2021) Rapid fluid-driven transformation of lower continental crust associated with thrust-induced shear heating. *Lithos*. <https://doi.org/10.1016/j.lithos.2021.106216>
- John T, Schenk V (2003) Partial eclogitization of gabbroic rocks in a late Precambrian subduction zone (Zambia): prograde metamorphism triggered by fluid infiltration. *Contrib Miner Petrol* 146(2):174–191. <https://doi.org/10.1007/s00410-003-0492-8>
- Jolivet L, Raimbourg H, Labrousse L, Avigad D, Leroy Y, Austrheim H, Andersen TB (2005) Softening triggered by eclogitization, the first step toward exhumation during continental subduction. *Earth Planet Sci Lett* 237(3–4):532–547. <https://doi.org/10.1016/j.epsl.2005.06.047>
- Kaatz L, Zertani S, Moulas E, John T, Labrousse L, Schmalholz SM, Andersen TB (2021) Widening of hydrous shear zones during incipient eclogitization of metastable dry and rigid lower crust—Holsnøy, Western Norway. *Tectonics* 40:e2020TC006572. <https://doi.org/10.1029/2020TC006572>
- Klemd R, John T, Scherer EE, Rondenay S, Gao J (2011) Changes in dip of subducted slabs at depth: Petrological and geochronological evidence from HP–UHP rocks (Tianshan, NW-China). *Earth Planet Sci Lett* 310(1–2):9–20. <https://doi.org/10.1016/j.epsl.2011.07.022>
- Locock AJ (2008) An Excel spreadsheet to recast analyses of garnet into end-member components, and a synopsis of the crystal chemistry of natural silicate garnets. *Comput Geosci* 34(12):1769–1780. <https://doi.org/10.1016/j.cageo.2007.12.013>
- Mancktelow NS (2002) Finite-element modelling of shear zone development in viscoelastic materials and its implications for localisation of partial melting. *J Struct Geol* 24(6):1045–1053. [https://doi.org/10.1016/S0191-8141\(01\)00090-6](https://doi.org/10.1016/S0191-8141(01)00090-6)
- Mancktelow NS, Pennacchioni G (2005) The control of precursor brittle fracture and fluid–rock interaction on the development of single and paired ductile shear zones. *J Struct Geol* 27(4):645–661. <https://doi.org/10.1016/j.jsg.2004.12.001>
- Manning CE, Ingebritsen SE (1999) Permeability of the continental crust: implications of geothermal data and metamorphic systems. *Rev Geophys* 37(1):127–150. <https://doi.org/10.1029/1998rg900002>
- Mattey D, Jackson DH, Harris NBW, Kelley S (1994) Isotopic constraints on fluid infiltration from an eclogite facies shear zone, Holsenøy, Norway. *J Metamorph Geol* 12(3):311–325. <https://doi.org/10.1111/j.1525-1314.1994.tb00025.x>
- Menegon L, Pennacchioni G, Malaspina N, Harris K, Wood E (2017) Earthquakes as precursors of ductile shear zones in the dry and strong lower crust. *Geochem Geophys Geosyst* 18(12):4356–4374. <https://doi.org/10.1002/2017GC007189>
- Moore J, Beinlich A, Austrheim H, Putnis A (2019) Stress orientation-dependent reactions during metamorphism. *Geology* 47(2):151–154. <https://doi.org/10.1130/G45632.1>
- Morimoto N (1988) Nomenclature of pyroxenes. *Mineral Petrol* 39:55–76. <https://doi.org/10.1007/bf01226262>

- Mørk MBE (1985) A gabbro to eclogite transition on Flemsøy, Sunnmøre, western Norway. *Chem Geol* 50(1–3):283–310. [https://doi.org/10.1016/0009-2541\(85\)90125-1](https://doi.org/10.1016/0009-2541(85)90125-1)
- Oliver NHS (1996) Review and classification of structural controls on fluid flow during regional metamorphism. *J Metamorph Geol* 14(4):477–492. <https://doi.org/10.1046/j.1525-1314.1996.00347.x>
- Pennacchioni G, Scambelluri M, Bestmann M, Notini L, Nimis P, Plümpner O, Faccenda M, Nestola F (2020) Record of intermediate-depth subduction seismicity in a dry slab from an exhumed ophiolite. *Earth Planet Sci Lett* 548:116490. <https://doi.org/10.1016/j.epsl.2020.116490>
- Petley-Ragan A, Dunkel KG, Austrheim H, Ildefonse B, Jamtveit B (2018) Microstructural records of earthquakes in the lower crust and associated fluid-driven metamorphism in plagioclase-rich granulites. *J Geophys Res Solid Earth* 123(5):3729–3746. <https://doi.org/10.1029/2017JB015348>
- Philpotts AR, Ague JJ (2022) Principles of igneous and metamorphic petrology. Cambridge University Press, Cambridge
- Plümpner O, Røyne A, Magrasó A, Jamtveit B (2012) The interface-scale mechanism of reaction-induced fracturing during serpentinization. *Geology* 40(12):1103–1106. <https://doi.org/10.1130/G33390.1>
- Plümpner O, Botan A, Los C, Liu Y, Malthe-Sørensen A, Jamtveit B (2017a) Fluid-driven metamorphism of the continental crust governed by nanoscale fluid flow. *Nat Geosci* 10:685–690. <https://doi.org/10.1038/ngeo3009>
- Plümpner O, John T, Podladchikov YY, Vrijmoed JC, Scambelluri M (2017b) Fluid escape from subduction zones controlled by channel-forming reactive porosity. *Nat Geosci* 10(2):150–156. <https://doi.org/10.1038/ngeo2865>
- Pollok K, Lloyd GE, Austrheim H, Putnis A (2008) Complex replacement patterns in garnets from Bergen Arcs eclogites: a combined EBSD and analytical TEM study. *Chem Erde* 68(2):177–191. <https://doi.org/10.1016/j.chemer.2007.12.002>
- Putnis A (2009) Mineral replacement reactions. *Rev Mineral Geochem* 70(1):87–124. <https://doi.org/10.2138/rmg.2009.70.3>
- Putnis A, Austrheim H (2010) Fluid-induced processes: metasomatism and metamorphism. *Geofluids* 10:254–269. <https://doi.org/10.1111/j.1468-8123.2010.00285.x>
- Putnis A, John T (2010) Replacement processes in the Earth's crust. *Elements* 6(3):159–164. <https://doi.org/10.2113/gselements.6.3.159>
- Putnis A, Moore J, Prent AM, Beinlich A, Austrheim H (2021) Preservation of granulite in a partially eclogitized terrane: Metastable phenomena or local pressure variations? *Lithos* 400–401:106413. <https://doi.org/10.1016/j.lithos.2021.106413>
- Raimbourg H, Jolivet L, Labrousse L, Leroy Y, Avigad D (2005) Kinematics of syneclogite deformation in the Bergen Arcs, Norway: implications for exhumation mechanisms. *Geol Soc Lond Spec Publ* 243:175–192. <https://doi.org/10.1144/gsl.sp.2005.243.01.13>
- Raimbourg H, Goffé B, Jolivet L (2007) Garnet reequilibration and growth in the eclogite facies and geodynamical evolution near peak metamorphic conditions. *Contrib Miner Petrol* 153:1–28. <https://doi.org/10.1007/s00410-006-0130-3>
- Rogowitz A, Huet B (2021) Evolution of fluid pathways during eclogitization and their impact on formation and deformation of eclogite: a microstructural and petrological investigation at the type locality (Koralpe, Eastern Alps, Austria). *Tectonophysics* 819:229079. <https://doi.org/10.1016/j.tecto.2021.229079>
- Rondenay S, Abers GA, van Keken PE (2008) Seismic imaging of subduction zone metamorphism. *Geology* 36(4):275–278. <https://doi.org/10.1130/G24112A.1>
- Schwarzenbach EM, Caddick MJ, Beard JS, Bodnar RJ (2016) Serpentinization, element transfer, and the progressive development of zoning in veins: evidence from a partially serpentinized harzburgite. *Contrib Miner Petrol* 171:5. <https://doi.org/10.1007/s00410-015-1219-3>
- Taetz S, John T, Bröcker M, Spandler C, Stracke A (2018) Fast intraslab fluid-flow events linked to pulses of high pore fluid pressure at the subducted plate interface. *Earth Planet Sci Lett* 482:33–43. <https://doi.org/10.1016/j.epsl.2017.10.044>
- Vrijmoed JC, Podladchikov YY (2015) Thermodynamic equilibrium at heterogeneous pressure. *Contrib Miner Petrol* 170:10. <https://doi.org/10.1007/s00410-015-1156-1>
- Vrijmoed JC, Podladchikov YY (2022) Thermolab: a thermodynamics laboratory for non-linear transport processes in open systems. *Earth Sp Sci Open Arch* 23:e2021GC010303. <https://doi.org/10.1002/essoar.10509513.1>
- Wassmann S, Stöckhert B (2013) Rheology of the plate interface—dissolution precipitation creep in high pressure metamorphic rocks. *Tectonophysics* 608:1–29. <https://doi.org/10.1016/j.tecto.2013.09.030>
- Wayte GJ, Worden RH, Rubie DC, Droop GTR (1989) A TEM study of disequilibrium plagioclase breakdown at high pressure: the role of infiltrating fluid. *Contrib Miner Petrol* 101(4):426–437. <https://doi.org/10.1007/bf00372216>
- Whitney DL, Evans BW (2010) Abbreviations of names of rock-forming minerals. *Am Miner* 95(1):185–187. <https://doi.org/10.2138/am.2010.3371>
- Wirth R, Kruhl JH, Morales LFG, Schreiber A (2021) Partially open grain and phase boundaries as fluid pathways in metamorphic and magmatic rocks. *J Metamorph Geol* 40:67–85. <https://doi.org/10.1111/jmg.12610>
- Zertani S, Labrousse L, John T, Andersen TB, Tilmann F (2019) The Interplay of Eclogitization and Deformation During Deep Burial of the Lower Continental Crust—A Case Study From the Bergen Arcs (Western Norway). *Tectonics* 38(3):898–915. <https://doi.org/10.1029/2018tc005297>
- Zertani S, Vrijmoed JC, Tilmann F, John T, Andersen TB, Labrousse L (2020) P wave anisotropy caused by partial eclogitization of descending crust demonstrated by modeling effective petrophysical properties. *Geochem Geophys Geosyst* 21(6):e2019GC008906. <https://doi.org/10.1029/2019gc008906>
- Zertani S, Pleuger J, Motra HB, John T (2022) Highly variable petrophysical properties in felsic high-pressure rocks of the continental crust. *Lithos* 410–411:106572. <https://doi.org/10.1016/j.lithos.2021.106572>
- Zhong X, Andersen NH, Dabrowski M, Jamtveit B (2019) Zircon and quartz inclusions in garnet used for complementary Raman thermobarometry: application to the Holsnøy eclogite, Bergen Arcs, Western Norway. *Contrib Miner Petrol* 174(6):50. <https://doi.org/10.1007/s00410-019-1584-4>

**Publisher's Note** Springer Nature remains neutral with regard to jurisdictional claims in published maps and institutional affiliations.